Geophysical Prospecting, 1996, **44**, 871–888

Ground radar simulation for archaeological applications[1]

José M. Carcione[2]

Abstract

This work presents a new modelling scheme for the simulation of electromagnetic radio waves, based on a full-field simulator. Maxwell's equations are modified in order to include dielectric attenuation processes, such as bound- and free-water relaxation, ice relaxation and the Maxwell–Wagner effect. The new equations are obtained by assuming a permittivity relaxation function represented by a generalized Zener model. The convolution integral introduced by the relaxation formulation is circumvented by defining new *hidden* field variables, each corresponding to a different dielectric relaxation. The equations are solved numerically by using the Fourier pseudospectral operator for computing the spatial derivatives and a new time-splitting integration algorithm that circumvents the stiffness of the differential equations. The program is used to evaluate the georadar electromagnetic response of a Japanese burial site, in particular, a stone coffin-like structure.

Introduction

The applications of ground-penetrating radar (GPR) as an ecological, high-resolution, non-destructive technique are widely documented. For a good review and state of the art see, for instance, Owen (1995).

Archaeological applications of electromagnetic (EM) methods include the work by Frohlich and Lancaster (1986), who used an EM induction meter to survey ancient Middle Eastern cemeteries, and Imai, Sakayama and Kanemori (1987) who conducted GPR and resistivity surveys to locate ancient Japanese dwellings, burial mounds and a distribution of archaeologically significant 'cultural' strata. Other applications include the search for buried remains of a 16th-century Basque whaling station on the Labrador coast (Vaughn 1986), the discovery of Roman foundations in Britain (Stove and Addyman 1989), and the search for graves in cemeteries and churches (Bevan 1991). More recently, Sternberg and McGill (1995) conducted successful GPR surveys in archaeological areas of southern Arizona. Integration of GPR measurements with seismic surveys has been applied by Brizzolari *et al.* (1992) to an archaeological site near Rome.

---

[1] Received July 1995, revision accepted December 1995.

[2] Osservatorio Geofisico Sperimentale, PO Box 2011, Opicina, 34016 Trieste, Italy.

EM numerical simulation in heterogeneous media is essential to validate the geological interpretations. GPR wave modelling is, in general, one-dimensional in the literature. Only very recently, Goodman (1994) proposed a two-dimensional wave-simulation method based on ray-tracing techniques. However, this approach suffers the disadvantages of ray methods, i.e. the impossibility of modelling the full wavefield at all frequency ranges (e.g. the complete set of multiples and diffractions), and the generation of non-uniform dissipative waves at material interfaces.

It is important to model the correct frequency dependence of the permittivity. At radar frequencies ($\approx$50 MHz–1 GHz), various dielectric dispersion processes occur. In moist soils, the most important are ionic conductivity and bound-water relaxation. The relaxation of the water molecule produces an increase in attenuation with frequency, since the molecules begin to lag the applied field and increase the real effective conductivity. This phenomenon is well described by a Debye relaxation peak, having its analogy in the Zener rheological model (also called the standard linear solid) used in viscoelasticity (e.g. Carcione 1990). Other less important processes that can be described by Debye mechanisms are the Maxwell–Wagner effect, surface conductivity at low frequencies and the two relaxations of free water at high frequencies. Moreover, at high frequencies, the response of free charges may lag the electric field and produce an out-of-phase component, contributing to the real effective permittivity. These phenomena, i.e. dielectric relaxation and out-of-phase electric currents, are introduced in Maxwell's equations by means of time-domain permittivity and conductivity functions.

Time-domain Maxwell's equations

In 3D vector notation, Maxwell's equations are (e.g. Chew 1990)

$$\nabla \times \mathbf{E} = -\frac{\partial \mathbf{B}}{\partial t} + \mathbf{M}, \tag{1}$$

$$\nabla \times \mathbf{H} = \frac{\partial \mathbf{D}}{\partial t} + \mathbf{J}, \tag{2}$$

where **E**, **B**, **H** and **D** are the electric intensity, the magnetic flux density, the magnetic intensity and the electric flux density, respectively, and **J** and **M** are the electric and magnetic current densities, respectively. In general, they depend on the Cartesian coordinates (x, y, z) and the time variable t. Equations (1) and (2) constitute six scalar equations with 12 scalar unknowns, since **J** and **M** are known. The six additional scalar equations are the constitutive relationships, which, for anisotropic media including dielectric relaxation, can be written as

$$\mathbf{D} = \epsilon * \frac{\partial \mathbf{E}}{\partial t}, \tag{3}$$

$$\mathbf{B} = \boldsymbol{\mu} \cdot \mathbf{H}, \tag{4}$$

where $\epsilon(\mathbf{x}, t)$ is the permittivity relaxation tensor and $\boldsymbol{\mu}(\mathbf{x})$ is the permeability tensor.

The symbol $*$ denotes time convolution, and the dot in the rhs of (4) denotes ordinary matrix multiplication. Moreover, the electric current density is given by the generalized Ohm's law

$$\mathbf{J} = \boldsymbol{\sigma} * \frac{\partial \mathbf{E}}{\partial t} + \mathbf{J}_\mathrm{s}, \tag{5}$$

where $\boldsymbol{\sigma}(\mathbf{x}, t)$ is the conductivity relaxation tensor and $\mathbf{J}_\mathrm{s}$ is the contribution of the sources. The first term of the rhs of (5) is the conduction current density, and the convolution accounts for out-of-phase components of the current with respect to the electric field. Substituting the constitutive relationships and the current density into (1) and (2), and using properties of the convolution, gives

$$\nabla \times \mathbf{E} = -\boldsymbol{\mu} \cdot \frac{\partial \mathbf{H}}{\partial t} + \mathbf{M}, \tag{6}$$

$$\nabla \times \mathbf{H} = \boldsymbol{\sigma} * \frac{\partial \mathbf{E}}{\partial t} + \boldsymbol{\epsilon} * \frac{\partial^2 \mathbf{E}}{\partial t^2} + \mathbf{J}_\mathrm{s}, \tag{7}$$

which corresponds to a system of six scalar equations in six scalar unknowns.

The TEM wave equation

Assume an isotropic medium, propagation in the (x, z)-plane, and that the material properties are constant with respect to the y-coordinate. Then, E_x, E_z and H_y are decoupled from E_y, H_x and H_z. The first three fields obey the TEM (transverse electric and magnetic fields) differential equations,

$$\frac{\partial E_z}{\partial x} - \frac{\partial E_x}{\partial z} = \mu \frac{\partial H_y}{\partial t} - M_y, \tag{8}$$

$$-\frac{\partial H_y}{\partial z} = \sigma * \frac{\partial E_x}{\partial t} + \epsilon * \frac{\partial^2 E_x}{\partial t^2} + \mathcal{J}_{\mathrm{s}x}, \tag{9}$$

$$\frac{\partial H_y}{\partial x} = \sigma * \frac{\partial E_z}{\partial t} + \epsilon * \frac{\partial^2 E_z}{\partial t^2} + \mathcal{J}_{\mathrm{s}z}, \tag{10}$$

where $\epsilon(t)$ and $\sigma(t)$ are the permittivity and conductivity relaxation functions, respectively, and μ is the magnetic permeability.

The relaxation functions

A realistic description of dielectric relaxation can be obtained by representing the permittivity with a generalized Debye model. This model accounts for many relaxation mechanisms that produce an out-of-phase component of the permittivity, such as atomic, molecular and volume polarization (King and Smith 1981). The permittivity relaxation function can be expressed as

$$\epsilon(t) = \epsilon^0 \left[1 - \frac{1}{L} \sum_{l=1}^{L} \left(1 - \frac{\lambda_l}{\tau_l} \right) \exp(-t/\tau_l) \right] \mathrm{H}(t), \tag{11}$$

where ϵ^0 is the static permittivity, λ_l and τ_l are relaxation times ($\lambda_l \leq \tau_l$) and L is the number of Debye relaxation mechanisms; $\mathrm{H}(t)$ is the Heaviside function. The condition $\lambda_l \leq \tau_l$ makes the relaxation function (11) analogous to the viscoelastic creep function of a series connection of standard linear solid elements (Casula and Carcione 1992). The optical or high-frequency permittivity is obtained for $t \rightarrow 0$. It gives

$$\epsilon^\infty = \frac{\epsilon^0}{L} \sum_{l=1}^{L} \frac{\lambda_l}{\tau_l}. \tag{12}$$

Note that $\epsilon^\infty \leq \epsilon^0$, always. On the other hand, the conductivity components are represented by a Kelvin–Voigt mechanical model analogue,

$$\sigma(t) = \sigma^0[\mathrm{H}(t) + \xi\delta(t)], \tag{13}$$

where σ^0 is the static conductivity, ξ is a relaxation time and $\delta(t)$ is the Dirac function. The out-of-phase component of the conduction current is quantified by the relaxation time ξ.

Introduction of the hidden variables

The TEM equations (8), (9) and (10) could be the basis for a numerical solution algorithm. However, the numerical evaluation of the convolution integrals is prohibitive when solving the differential equations with grid methods and explicit time-evolution techniques. The conductivity terms pose no problems, since the substitution of the conductivity relaxation components into (9) and (10) does not involve time convolutions (see (19) below). In order to circumvent the convolutions due to the permittivity components, a new set of field variables is introduced.

Let us consider, for instance, the term $\epsilon * \partial^2 E_m/\partial t^2$ in (9) and (10), where $m = 1$ and $m = 3$ are used to denote the x- and z-components of the electric field, respectively. With the use of (11) and (12), and convolution properties (in particular, given $f(t)$ and $g(t)$, the following relationships hold: $f'\delta * g = f'(0)g$, and $f\delta' * g = f(0)g' - f'(0)g$), the convolution terms can be written as

$$\epsilon * \frac{\partial^2 E_m}{\partial t^2} = \frac{\partial^2 \epsilon}{\partial t^2} * E_m = \epsilon^\infty \frac{\partial E_m}{\partial t} + \epsilon^0 \sum_{l=1}^{L} \phi_l(0) E_m - \epsilon^0 \sum_{l=1}^{L} \frac{1}{\tau_l} \phi_l * E_m, \tag{14}$$

where

$$\phi_l(t) = \frac{\mathrm{H}(t)}{L\tau_l} \left(1 - \frac{\lambda_l}{\tau_l} \right) \exp(-t/\tau_l), \qquad l = 1, \ldots, L. \tag{15}$$

Defining the *hidden* field variables as

$$e_l^{(m)} = -\frac{1}{\tau_l}\phi_l * E_m, \qquad l = 1, \ldots, L, \tag{16}$$

(14) takes the form

$$\epsilon * \frac{\partial^2 E_m}{\partial t^2} = \epsilon^\infty \frac{\partial E_m}{\partial t} + \epsilon^0 \left[\Phi E_m + \sum_{l=1}^{L} e_l^{(m)}\right], \tag{17}$$

where

$$\Phi = \sum_{l=1}^{L} \phi_l(0). \tag{18}$$

The hidden variables introduced here are the analogue of the memory variables used in viscoelastic wave simulation to describe dissipation due to different relaxation processes (see Carcione 1990, 1993).

The wave equation

From (13), the conductivity terms in the rhs of (9) and (10) become

$$\sigma * \frac{\partial E_m}{\partial t} = \sigma^0 \left(E_m + \xi \frac{\partial E_m}{\partial t}\right). \tag{19}$$

Substituting (17) and (19) into (9) and (10) gives

$$-\frac{\partial H_y}{\partial z} = \sigma_e E_x + \epsilon_e \frac{\partial E_x}{\partial t} + \epsilon^0 \sum_{l=1}^{L} e_l^{(x)} + \mathcal{J}_{sx} \tag{20}$$

and

$$\frac{\partial H_y}{\partial x} = \sigma_e E_z + \epsilon_e \frac{\partial E_z}{\partial t} + \epsilon^0 \sum_{l=1}^{L} e_l^{(z)} + \mathcal{J}_{sz}, \tag{21}$$

where

$$\epsilon_e^\infty = \epsilon^\infty + \sigma^0 \xi \tag{22}$$

and

$$\sigma_e^\infty = \sigma^0 + \epsilon^0 \Phi \tag{23}$$

are the effective optical permittivity and conductivity, respectively.

The first two terms on the rhs of (20) and (21) correspond to the instantaneous response of the medium, as can be inferred from the relaxation functions (11) and (13). Note that the terms containing the conductivity relaxation time ξ are in phase with the instantaneous polarization response. The last term in each equation involves the relaxation processes through the hidden variables.

The wave equation is completed with the differential equations corresponding to the hidden variables. Time differentiation of (16) and the use of convolution properties yield

$$\frac{\partial e_l^{(m)}}{\partial t} = -\frac{1}{\tau_l}[e_l^{(m)} + \phi_l(0)E_m]. \tag{24}$$

Equations (8), (20), (21) and (24) give the EM response of a conducting medium with dielectric relaxation behaviour and out-of-phase conduction currents. These equations are the basis of the numerical algorithm, described in the last section, to obtain the field vector $[H_y, E_x, E_z, e_l^{(m)}]$, $i, m = 1$ or 3. A similar set of equations, but without Debye relaxations mechanisms and out-of-phase currents, are given by Carcione and Cavallini (1994).

Plane-wave theory

In the absence of magnetic moments, the time Fourier transform of (8) is

$$\nabla_2^{\mathrm{T}} \cdot \mathbf{E} = \mathrm{i}\omega\mu H_y, \tag{25}$$

where $\mathbf{E} = [E_x, E_z]^{\mathrm{T}}$ and $\nabla_2 = [-\partial/\partial z, \partial/\partial x]^{\mathrm{T}}$. Equations (9) and (10), in the absence of electric current sources, can be written in compact form as

$$\nabla_2 H_y = \frac{\partial \sigma}{\partial t} * \mathbf{E} + \frac{\partial \epsilon}{\partial t} * \frac{\partial \mathbf{E}}{\partial t}. \tag{26}$$

Using the convolution theorem, (26) becomes

$$\nabla_2 H_y = \mathrm{i}\omega\left(\tilde{\epsilon} - \frac{\mathrm{i}}{\omega}\tilde{\sigma}\right)\mathbf{E} = \mathrm{i}\omega\left(\epsilon_{\mathrm{e}} - \frac{\mathrm{i}}{\omega}\sigma_{\mathrm{e}}\right)\mathbf{E}, \tag{27}$$

where

$$\epsilon_{\mathrm{e}} = \Re(\tilde{\epsilon}) + \frac{1}{\omega}\Im(\tilde{\sigma}) \tag{28}$$

and

$$\sigma_{\mathrm{e}} = \Re(\tilde{\sigma}) - \omega\Im(\tilde{\epsilon}) \tag{29}$$

are the real effective permittivity and conductivity, respectively, and the operators $\Re(\cdot)$ and $\Im(\cdot)$ take the real and imaginary parts, respectively. Moreover,

$$\tilde{\epsilon} = \mathcal{F}\left[\frac{\partial \epsilon}{\partial t}\right] = \frac{\epsilon^0}{L}\sum_{l=1}^{L}\frac{1 + \mathrm{i}\omega\lambda_l}{1 + \mathrm{i}\omega\tau_l} \tag{30}$$

and

$$\tilde{\sigma} = \mathcal{F}\left[\frac{\partial \sigma}{\partial t}\right] = \sigma^0(1 + \mathrm{i}\omega\xi), \tag{31}$$

with the operator $\mathcal{F}$ denoting time Fourier transform. Since $\lambda_l \leq \tau_l$ implies $\Im(\tilde{\epsilon}) \leq 0$ and $\Re(\tilde{\sigma}) \geq 0$, the two terms on the rhs of (29) have the same sign and the wave processes are always dissipative. The importance of the effective properties is that they are measurable quantities; ϵ_e produces a current that is out-of-phase with the electric field, while σ_e produces a current that varies in phase with the electric field.

Multiplying (27) from the left by $\beta \nabla_2^T$, where

$$\beta = \left(\epsilon_e - \frac{i}{\omega}\sigma_e\right)^{-1} \tag{32}$$

is the (effective) dielectric impermeability, and substituting (25), gives

$$\Delta H_y + \frac{\mu}{\beta}\omega^2 H_y = 0, \tag{33}$$

where Δ is the Laplacian operator.

The magnetic field associated with a uniform TEM plane wave has the form

$$\mathbf{H} = H_y \mathbf{e}_2, \qquad H_y \equiv H_0 \exp\left[-ik\hat{\boldsymbol{\kappa}}^T \cdot \mathbf{x}\right], \qquad \mathbf{e}_2 \equiv [0, 1, 0]^T, \tag{34}$$

where $\mathbf{x} = [x, z]^T$,

$$k = \kappa - i\alpha \tag{35}$$

is the complex wavenumber, where κ and α are the magnitudes of the real propagation and attenuation vectors, respectively, H_0 is a complex constant, and

$$\hat{\boldsymbol{\kappa}} = [l_x, l_z]^T \tag{36}$$

defines the propagation (and attenuation) direction through the direction cosines l_x and l_z. Since, for the plane wave (34),

$$\nabla_2 = -i\mathbf{K}_2, \qquad \mathbf{K}_2 = k[-l_z, l_x]^T, \tag{37}$$

the substitution of (37) into (33) gives the dispersion relationship

$$\beta - \mu\left(\frac{\omega}{k}\right)^2 = 0. \tag{38}$$

The dispersion relationship defines the complex velocity

$$V \equiv \frac{\omega}{k} = \sqrt{\frac{\beta}{\mu}}. \tag{39}$$

The real attenuation and slowness vectors can be expressed in terms of the complex velocity as

$$\boldsymbol{\alpha} = -\omega\Im\left(\frac{1}{V}\right)\hat{\boldsymbol{\kappa}} \tag{40}$$

and

$$\mathbf{s} \equiv \frac{\kappa}{\omega}\hat{\boldsymbol{\kappa}} = \Re\left(\frac{1}{V}\right)\hat{\boldsymbol{\kappa}}, \tag{41}$$

while the phase velocity is, in magnitude, the reciprocal of the slowness and, in vector form, is given by

$$\mathbf{V}_p = \left[\Re\left(\frac{1}{V}\right)\right]^{-1}\hat{\kappa}. \tag{42}$$

The energy velocity is the ratio between the average power flow and the mean energy density. It can be shown that in isotropic lossy media, the energy velocity equals the phase velocity. Another important quantity is the quality factor. This quantifies, somehow, energy dissipation in matter from the electric current standpoint. As stated by Harrington (1961, p. 28), the quality factor is defined as the ratio of the magnitude of reactive current density to the magnitude of dissipative current density. In viscoelastodynamics, a common definition of quality factor is twice the ratio of the average potential energy density to the dissipated energy density. Accordingly, and using the acoustic-electromagnetic analogy (Carcione and Cavallini 1995), the quality factor is defined here as twice the ratio of the average electric energy to the density of energy dissipated in one cycle. It can be shown that the quality factor is given by

$$Q = \frac{\Re(V^2)}{\Im(V^2)}. \tag{43}$$

The concept of the quality factor can be considered as a generalization of the concept

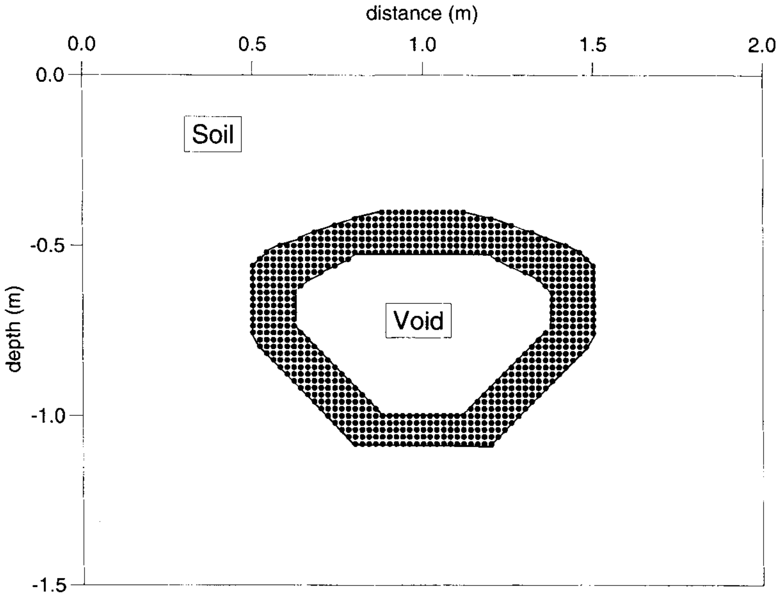

Figure 1. Model representing a coffin-like structure found at the Kofun period (300–700 A.D.) burial mounds in Japan (after Goodman and Nishimura 1993).

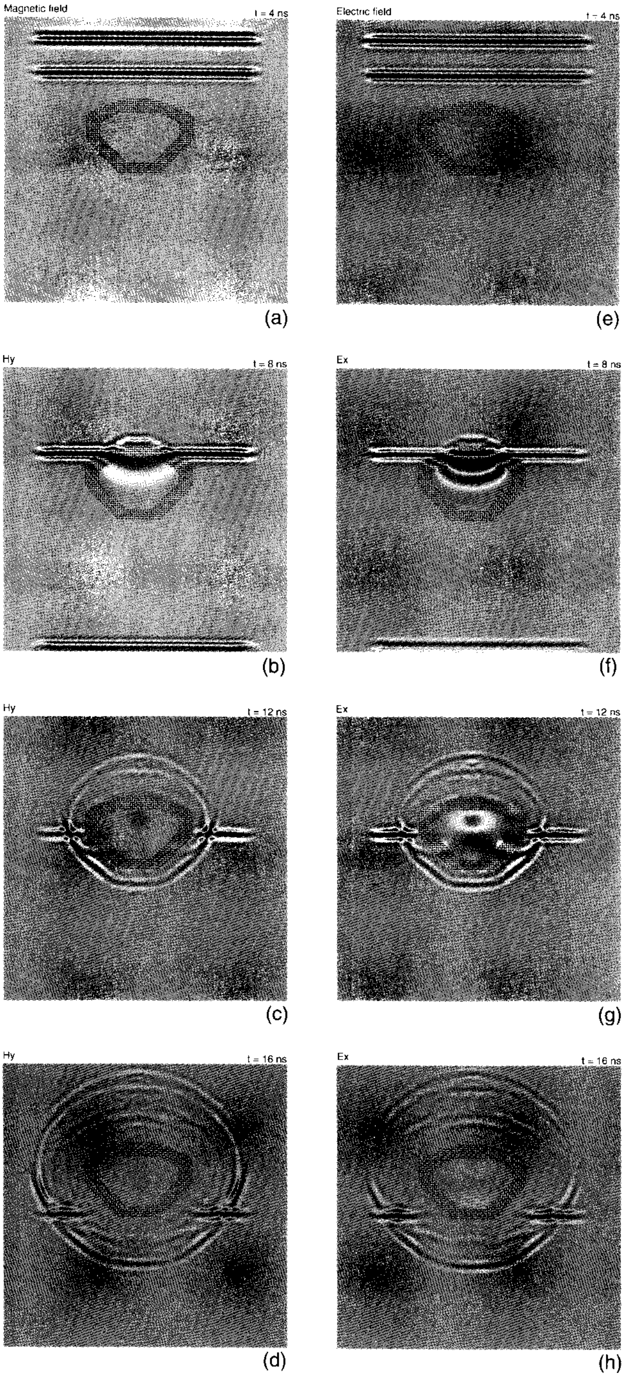

Figure 2. Sequence of snapshots corresponding to the magnetic field H_y and the electric-field component E_x. The void is filled with air. The source is a horizontal electric current (plane wave) and its dominant frequency is 800 MHz.

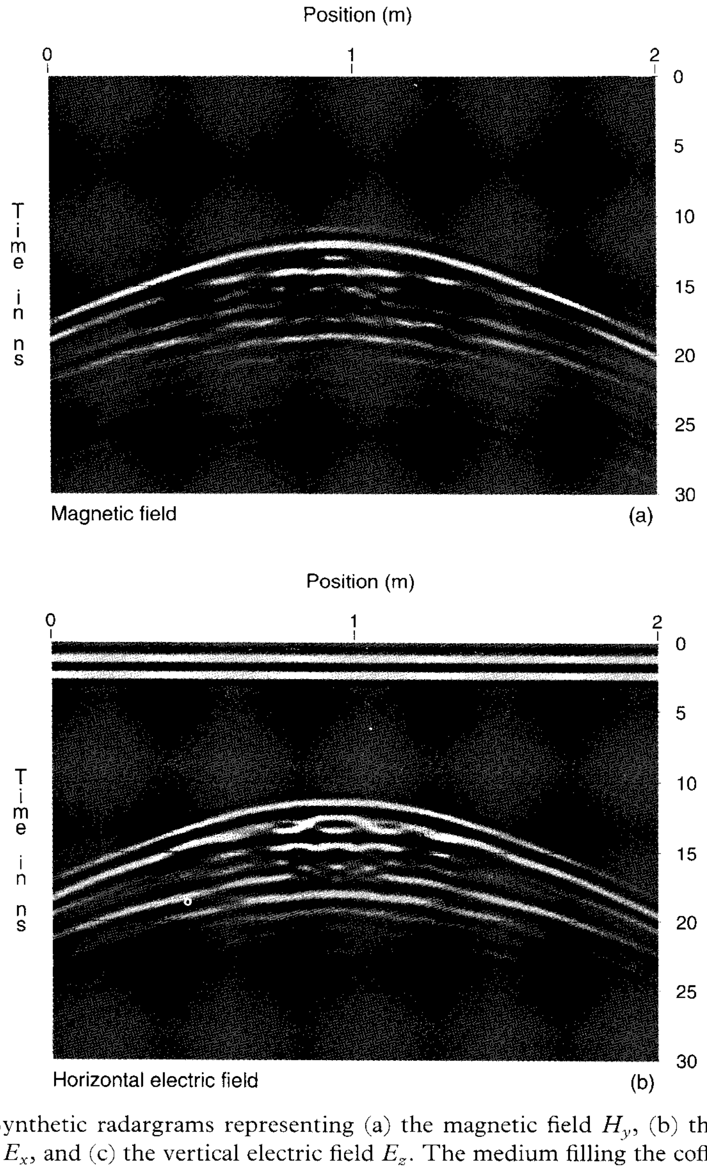

Figure 3. Synthetic radargrams representing (a) the magnetic field H_y, (b) the horizontal electric field E_x, and (c) the vertical electric field E_z. The medium filling the coffin is air.

of Q in circuit theory. Good dielectrics have high Q values and conductors have very low Q values.

Numerical algorithm

In order to illustrate the numerical solution algorithm, the equations with one dielectric relaxation mechanism are considered. Equations (8), (20), (21) and (24) can

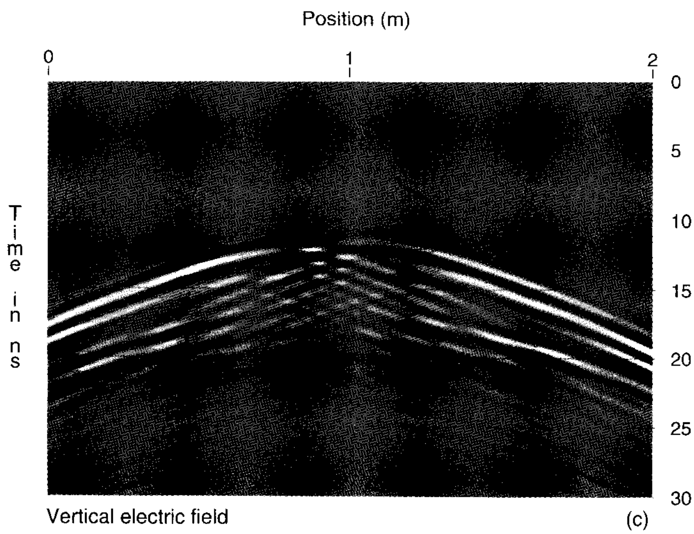

Figure 3. Continued.

be written in compact matrix form as

$$\frac{\partial \mathbf{V}}{\partial t} = \mathbf{MV} + \mathbf{S}, \tag{44}$$

where

$$\mathbf{V} = [H_y, E_x, E_z, e_x, e_z]^{\mathrm{T}} \tag{45}$$

is the unknown vector field, and

$$\mathbf{M} = \begin{bmatrix} 0 & -\mu^{-1}\partial_z & \mu^{-1}\partial_x & 0 & 0 \\ -(\epsilon_{\mathrm{e}}^{\infty})^{-1}\partial_z & -(\epsilon_{\mathrm{e}}^{\infty})^{-1}\sigma_{\mathrm{e}}^{\infty} & 0 & -(\epsilon_{\mathrm{e}}^{\infty})^{-1}\epsilon^0 & 0 \\ (\epsilon_{\mathrm{e}}^{\infty})^{-1}\partial_x & 0 & -(\epsilon_{\mathrm{e}}^{\infty})^{-1}\sigma_{\mathrm{e}}^{\infty} & 0 & -(\epsilon_{\mathrm{e}}^{\infty})^{-1}\epsilon^0 \\ 0 & -\Phi/\tau & 0 & -\tau^{-1} & 0 \\ 0 & 0 & -\Phi/\tau & 0 & -\tau^{-1} \end{bmatrix}, \tag{46}$$

where ∂_x and ∂_z denote spatial derivatives.

Equation (44) is solved with a direct grid method that computes the spatial derivatives by using the Fourier pseudospectral method (e.g. Canuto *et al.* 1988) and propagates the solution in time with a fourth-order Runge–Kutta algorithm. However, when there is a Debye peak whose central frequency is much larger than the dominant frequency of the source, the equations become stiff (Jain 1984). In this case, a partition (or splitting) time integrator algorithm is used. The stiff part is solved analytically and the non-stiff part is solved by an explicit Runge–Kutta algorithm (see Appendix). The modelling improves significantly with this

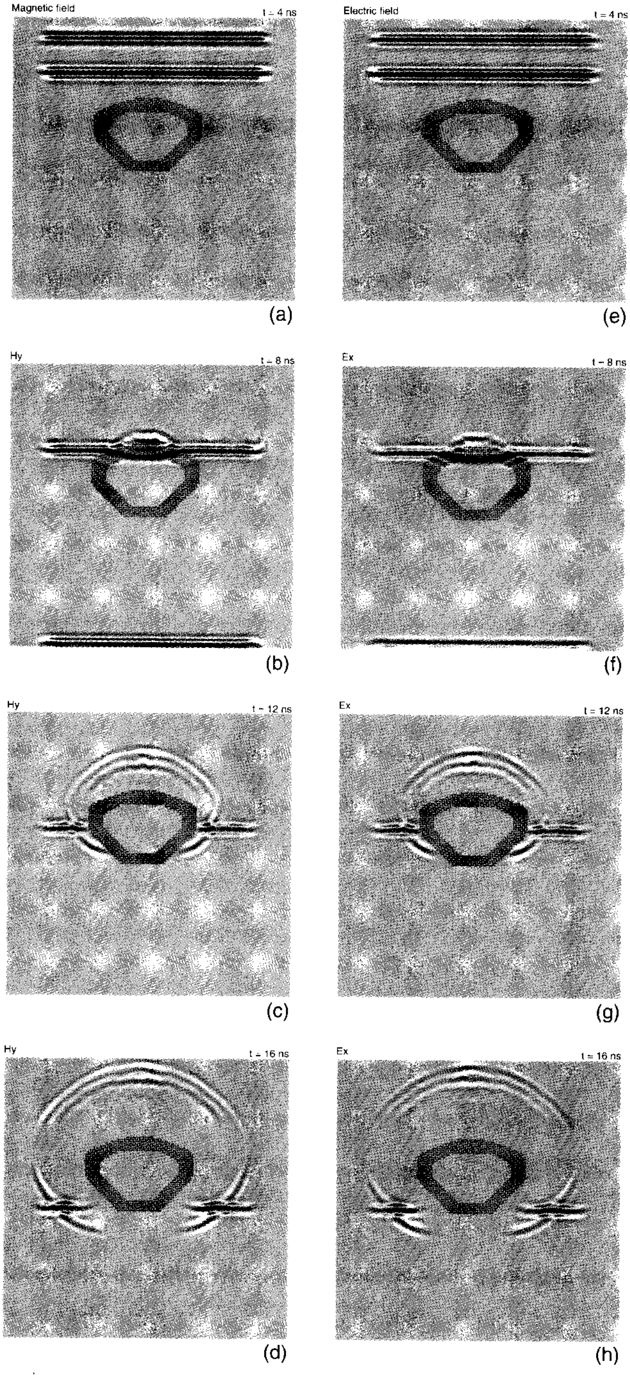

Figure 4. Sequence of snapshots corresponding to the magnetic field H_y and the electric-field component E_x. The void is filled with salt water.

approach. However, a better technique in terms of numerical stability, such as an implicit algorithm, should further improve its performance. A modelling software package, GEMS (Georadar Electromagnetic Modelling and Simulation), has been developed, which designs the geological model, provides the kinematic and dynamic properties of each medium, and generates the radargrams for a variety of antenna configurations.

Example: Japanese burial site

The simulation is based on a study conducted by Goodman and Nishimura (1993) which used the GPR method to survey protected burial mounds in Japan. One particular burial style, belonging to the Kofun period (300–700 A.D.), is shown in Fig. 1, where a cross-section of a stone coffin is represented (the dots correspond to gridpoints of the numerical mesh). The soil and the coffin have a dielectric constant of $16\epsilon_0$ and $4\epsilon_0$, respectively, where $\epsilon_0 = 8.85\ 10^{-12}$ F/m. The magnetic permeability μ has been taken equal to that of a vacuum ($\mu_0 = 4\pi\ 10^{-7}$ H/m). A first simulation considers the coffin filled with air. The numerical mesh has $N_X = N_Z = 135$ gridpoints per side, with a uniform grid spacing of $D_X = D_Z = 2$ cm. Absorbing strips of length 18 gridpoints are used at the boundaries of the mesh to eliminate wrap-around effects produced by the Fourier differential operator. The field is initiated at gridpoint 40 by a horizontal electric current with a central frequency of 800 MHz, and is propagated with a time step of 0.02 ns. The receivers are located at the same level of the source. The experiment simulates a stacked radargram obtained from the processing of a series of common-'shot' gathers. Figure 2 shows a series of snapshots corresponding to the magnetic field H_y and the electric-field component E_x. At 8 ns the field has penetrated the coffin; there is a reflection from the top and a transmitted wave that has a longer wavelength due to the difference in phase velocities. The snapshots at 12 and 16 ns indicate that three reflections, generated by the top and bottom of the coffin, are the principal events. In fact, they can be appreciated in the synthetic radargrams shown in Fig. 3, where (a) is the magnetic field H_y, (b) is the electric-field component E_x and (c) is the electric-field component E_z. Between the reflections, a complicated interference pattern is produced by reverberations inside the coffin. A similar radargram was computed by Goodman (1994) using ray-tracing methods.

The second simulation considers that the void is filled with salt water. For this, it is assumed that $\sigma^0 = 3 \times 10^{-3}$ mho/m, and that there is a dielectric relaxation centred at 1 GHz, defined by $\epsilon^\infty = 4.3\epsilon_0$, $\tau = 0.67$ ns and $\lambda = 3.75 \times 10^{-2}$ ns. This gives a static dielectric constant $\epsilon^0 = 77.16\epsilon_0$, a quality factor of 1.6 and a phase velocity of 3.8 cm/ns at 800 MHz. Figure 4 shows a sequence of snapshots and Fig. 5 displays the corresponding radargrams. The high dissipation produced by the salt water has eliminated the reflection coming from the bottom of the coffin. Moreover, as can be appreciated in Fig. 4, there is practically no energy transmission below the object.

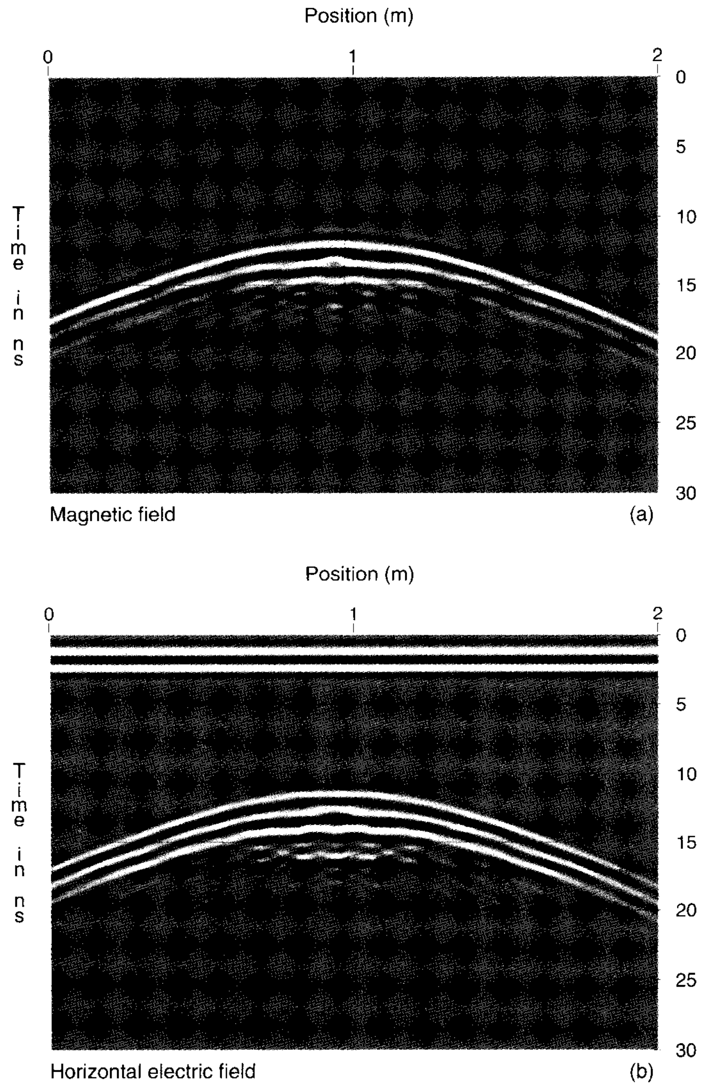

Figure 5. Synthetic radargrams representing (a) the magnetic field H_y, (b) the horizontal electric field E_x, and (c) the vertical electric field E_z. The medium filling the coffin is salt water.

Conclusions

The present modelling technique uses a time-dependent formulation of the dielectric and conductivity properties, which accounts for the various dissipation mechanisms of the radio-frequency band. In particular, the Debye relaxations require the introduction of hidden variables that are solved together with the electric and magnetic fields. A plane-wave analysis, based on uniform plane waves, gives the

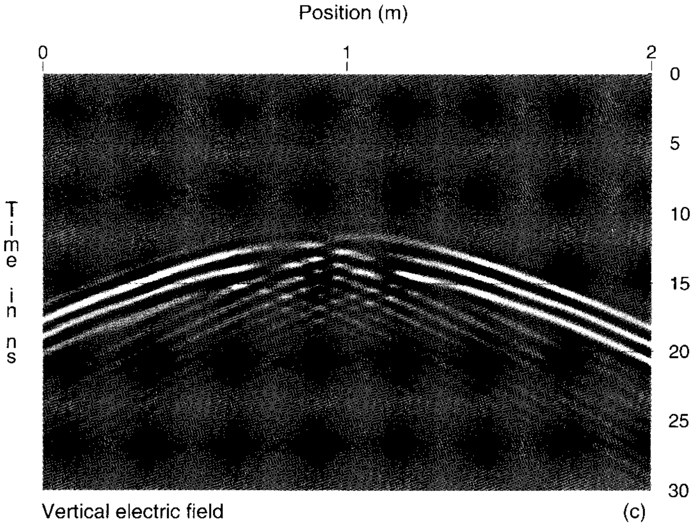

Figure 5. Continued.

expressions of measurable quantities, such as the quality factor and the phase and energy velocities, as a function of the frequency. The numerical modelling is based on the Fourier differential operator, and allows the calculation of the complete wavefield in arbitrarily inhomogeneous media. The stiffness of the differential equations (caused by the relaxation processes) is handled with a time-splitting integration algorithm.

A numerical simulation of a burial site shows how the modelling can be used as an interpretation tool. The nature of the wavefield can be determined by computing snapshots at any propagation time. In this way, the reflections observed in the radargram can be easily interpreted.

Acknowledgements

This work was funded in part by AGIP S.p.A. and the European Commission in the framework of the JOULE programme, sub-programme Advanced Fuel Technologies.

Appendix
Time integration for stiff electromagnetic equations

Assume an electromagnetic wave travelling in the x-direction with the magnetic and electric fields polarized in the y- and z-directions, respectively. When using the Fourier pseudospectral method, the wavenumbers κ supported by the numerical mesh span from zero to the Nyquist wavenumber π/D_X, where D_X is the grid spacing. In the wavenumber domain, the eigenvalues $\gamma = \mathrm{i}\omega$ (ω complex) of matrix **M** satisfy the characteristic equation,

$$\gamma\left[\left(\gamma + \frac{\sigma_\mathrm{e}^\infty}{\epsilon_\mathrm{e}^\infty}\right)\left(\gamma + \frac{1}{\tau}\right) - \frac{\Phi\epsilon^0}{\tau\epsilon_\mathrm{e}^\infty}\right] + \left(\gamma + \frac{1}{\tau}\right)\frac{\kappa^2}{\mu\epsilon_\mathrm{e}^\infty} = 0, \tag{A1}$$

where $\sigma_\mathrm{e}^\infty = \sigma^0 + \epsilon^0\Phi$ and $\epsilon_\mathrm{e}^\infty = \epsilon^\infty + \sigma^0\xi$. When $\lambda = \tau$ and $\sigma_\mathrm{e}^\infty = 0$, $\gamma = \pm\mathrm{i}V_\mathrm{p}\kappa$, where $V_\mathrm{p} = 1/\sqrt{\epsilon_\mathrm{e}^\infty\mu}$ is the phase velocity. In this case, the eigenvalues lie on the imaginary axis. On the other hand, the general solution of (A1) gives a static mode corresponding to a real and negative eigenvalue λ_s, and two propagating modes lying close to the imaginary axis, corresponding to the other eigenvalues. When the central frequency of a Debye peak is much larger than the dominant frequency of the source, $\lambda_\mathrm{s} \approx -1/\lambda$, and its magnitude is much larger than the eigenvalues corresponding to the propagating modes. In order to have numerical stability, the domain of convergence of the time-integration scheme should include the static eigenvalue. For instance, an explicit 4th-order Runge–Kutta method requires $dt\lambda_\mathrm{s} > -2.78$, implying a very small time step dt. In this case, the method is restricted by numerical stability rather than by accuracy. The presence of this large eigenvalue, together with small eigenvalues, indicates that the problem is stiff (Jain 1984, p. 72).

The system of electromagnetic equations can be partitioned into two sets of differential equations, one stiff and the other non-stiff. Consider, for instance (20) and (24). The stiff part is

$$\frac{\partial E_x}{\partial t} = -\frac{\epsilon^0}{\epsilon_\mathrm{e}^\infty} e_x, \tag{A2}$$

$$\frac{\partial e_x}{\partial t} = -\frac{1}{\tau}[e_x + \Phi E_x]. \tag{A3}$$

Now, assume that the solution at time ndt is E_x^n, e_x^n and $\partial e_x^n/\partial t = -(e_x^n + \Phi E_x^n)/\tau$. The solution at an intermediate time, labelled by an asterisk, can be obtained in analytical form. It yields

$$e_x^* = A\exp(\lambda_1 t) + B\exp(\lambda_2 t), \tag{A4}$$

$$E_x^* = E_x^n - \frac{\epsilon^0}{\epsilon_\mathrm{e}^\infty}\left\{\frac{A}{\lambda_1}[\exp(\lambda_1) - 1] + \frac{B}{\lambda_2}[\exp(\lambda_2) - 1]\right\}, \tag{A5}$$

where

$$\lambda_1 = -(\tau^{-1} + \Theta)/2, \qquad \lambda_2 = -(\tau^{-1} - \Theta)/2, \tag{A6}$$

with

$$\Theta = \frac{1}{\tau}\left[1 + 4\left(\frac{\epsilon^0 - \epsilon^\infty}{\epsilon_\mathrm{e}^\infty}\right)\right]^{1/2}, \tag{A7}$$

and

$$A = -\frac{1}{\Theta}\left(\frac{\partial e_x^n}{\partial t} - e_x^n \lambda_2\right), \qquad B = \frac{1}{\Theta}\left(\frac{\partial e_x^n}{\partial t} - e_x^n \lambda_1\right). \tag{A8}$$

Similar equations are obtained for the z-component. The intermediate vector,

$$\mathbf{V}^* = [H_y^n, E_x^*, E_z^*, e_x^*, e_z^*]^{\mathrm{T}}, \tag{A9}$$

is the input for an explicit fourth-order Runge–Kutta algorithm that solves the non-stiff part of (44), to give the solution at time $(n+1)dt$. A similar partition algorithm for solving Biot's poroelastic equations was developed by Carcione and Quiroga–Goode (1995).

References

Bevan B.W. 1991. The search for graves. *Geophysics* **56**, 1310–1319.

Brizzolari E., Ermolli F., Orlando L., Piro S. and Versino L. 1992. Integrated geophysical methods in archaeological surveys. *Journal of Applied Geophysics*, **29**, 47–55.

Canuto C., Hussaini M.Y., Quarteroni A. and Zang T.A. 1988. *Spectral Methods in Fluid Dynamics*. Springer Verlag, Inc.

Carcione J.M. 1990. Wave propagation in anisotropic linear viscoelastic media: theory and simulated wavefields. *Geophysics Journal International* **101**, 739–750. Erratum: **111**, 191.

Carcione J.M. 1993. Seismic modeling in viscoelastic media. *Geophysics* **58**, 110–120.

Carcione J.M. and Cavallini F. 1994. Modeling transverse electromagnetic waves in conducting anisotropic media by a spectral time-domain technique. In: 10th Annual Review of Progress in Applied Computational Electromagnetics (ed. A. Terzuoli), Vol. **II**, 586–593, Monterey CA.

Carcione J.M. and Cavallini F. 1995. On the acoustic-electromagnetic analogy. *Wave Motion* **21**, 149–162.

Carcione J.M. and Quiroga-Goode G. 1995. Some aspects of the physics and numerical modeling of Biot compressional waves. *Journal of Computational Acoustics* **3**, 261–280.

Casula G. and Carcione J.M. 1992. Generalized mechanical model analogies of linear viscoelastic behaviour. *Bolletino di Geofisica Teorica ed Applicata* **34**, 235–256.

Chew W.C. 1990. *Waves and Fields in Inhomogeneous Media*. Van Nostrand Reinhold Co.

Frohlich B. and Lancaster W.J. 1986. Electromagnetic surveying in current Middle Eastern archaeology: Application and evaluation. *Geophysics* **51**, 1414–1425.

Goodman D. 1994. Ground-penetrating radar simulation in engineering and archaeology. *Geophysics* **59**, 224–232.

Goodman D. and Nishimura Y. 1993. A ground-radar view of Japanese burial mounds. *Antiquity* **67**, 349–354.

Harrington R.F. 1961. *Time-Harmonic Electromagnetic Fields*. McGraw–Hill Book Co.

Imai T., Sakayama T. and Kanemori T. 1987. Use of ground-penetrating radar and resistivity surveys for archaeological investigations. *Geophysics* **52**, 137–150.

Jain M.K. 1984. *Numerical Solutions of Partial Differential Equations*. Wiley Eastern Ltd.

King R.W.P. and Smith G.S. 1981. *Antennas in Matter*. M.I.T. Press.

Owen T.E. (editor). 1995. Special Issue on Ground Penetrating Radar. *Journal of Applied Geophysics* **33**, 1–255.

Sternberg B.K. and McGill J.W. 1995. Archaeology studies in southern Arizona using ground penetrating radar. *Journal of Applied Geophysics* **33**, 209–255.

Stove G.C. and Addyman P.V. 1989. Ground probing impulse radar: an experiment in archaeological remote sensing at York. *Antiquity* **63**, 337–342.

Vaughn C.J. 1986. Ground-penetrating radar surveys used in archaeological investigations. *Geophysics* **51**, 595–604.